Nanoscale

ROYAL SOCIETY OF CHEMISTRY

PAPER

View Article Online
View Journal | View Issue

Cite this: *Nanoscale*, 2022, **14**, 13755

All-colloidal parity–time-symmetric microfiber lasers balanced between the gain of colloidal quantum wells and the loss of colloidal metal nanoparticles†

Sina Foroutan-Barenji,[a] Farzan Shabani,[a] Ahmet Tarik Isik,[a] Zeynep Dikmen[a,b] and Hilmi Volkan Demir *[c]

Lasers based on semiconductor colloidal quantum wells (CQWs) have attracted wide attention, thanks to their facile solution-processability, low threshold and wide range spectral tunability. Colloidal microlasers based on whispering-gallery-mode (WGM) resonators have already been widely demonstrated. However, due to their microscale size typically supporting multiple modes, they suffer from multimode competition and higher threshold. The ability to control the multiplicity of modes oscillating within colloidal laser resonators and achieving single-mode lasers is of fundamental importance in many photonic applications. Here we show that as a unique, simple and versatile architecture of all-colloidal lasers intrinsically enabled by balanced gain/loss segments, the lasing threshold reduction and spectral purification can be readily achieved in a system of a WGM-supported microfiber cavity by harnessing the notions of parity–time symmetry (PT). In particular, we demonstrate a proof-of-concept PT-symmetric microfiber laser employing CQWs as the colloidal gain medium along with a carefully tuned nanocomposite of Ag nanoparticles (Ag NPs) incorporated into a PMMA matrix altogether and conveniently coated around a coreless microfiber as a rigorously tailored colloidal loss medium to balance the gain. The realization of gain/loss segments in our PT-symmetric all-colloidal arrangement is independent of selected pumping, reducing the complexity of the system and making compact device applications feasible, where control over the pumping is not possible. We observed a reduction in the number of modes, resulting in a reduced threshold and enhanced output power of the PT-symmetric laser. The PT-symmetric CQW-WGM microcavity architecture offers new opportunities towards simple implementation of high-performance optical resonators for colloidal lasers.

Received 19th April 2022,
Accepted 23rd August 2022

DOI: 10.1039/d2nr02146c

rsc.li/nanoscale

Introduction

Lasers based on solution-processed materials have attracted intensive scientific and technological interest owing to their unique advantages including low-cost synthesis and processability and precise control of the emission wavelength enabling lasing in different colors.[1,2] Among solution-processable materials thus far studied for lasing applications, CQWs have gained considerable attention recently thanks to their attractive properties including large absorption cross-section,[3] giant oscillator strength,[4] giant gain cross-section,[5] large material gain coefficient,[6] and ultra-narrow emission spectra resulting from suppressed inhomogeneous broadening due to synthetic control over the vertical thickness of CQWs in the ensemble.[7] Previously, various heterostructures of CQWs have been used as active media in optical gain and laser applications, integrating their closely packed solid films into various optical resonator structures. These specifically include active waveguides,[8]

[a]*Department of Electrical and Electronics Engineering, Department of Physics, UNAM – Institute of Materials Science and Nanotechnology, Bilkent University, Ankara 06800, Turkey. E-mail: volkan@bilkent.edu.tr*
[b]*Faculty of Engineering, Department of Biomedical Engineering, Osmangazi University, Eskisehir 26040, Turkey*
[c]*LUMINOUS! Centre of Excellence for Semiconductor Lighting and Displays, Centre of Optical fiber Technology, The Photonics Institute, School of Electrical and Electronic Engineering, School of Physical and Mathematical Sciences, School of Materials Science and Engineering, Nanyang Technological University, 50 Nanyang Avenue, Singapore 639798, Singapore. E-mail: hvdemir@ntu.edu.sg*

†Electronic supplementary information (ESI) available: Description of FDTD and frequency domain eigen mode simulations, chemicals and materials, synthesis procedures, refractive index measurement using ellipsometry, dip-coating of the nanocomposite and CQWs around the coreless microfiber, and details of the lasing measurements. Demonstration of the 3D PL image of the coated coreless microfiber (AVI). See DOI: https://doi.org/10.1039/d2nr02146c

vertical-cavity surface-emitting lasers,[9,10] on-chip cavities,[11] and WGM resonators.[12,13]

One of the main challenges in the development of laser cavity configurations is to design a high quality-factor (Q-factor) and large resonant mode overlapping with the gain medium (Γ).[14] Large Q and Γ can result in strong coupling between the active material and cavity resonance mode, which paves the way for a narrow linewidth and low-threshold lasers.[15,16] WGM resonators have been found to be highly efficient optical cavities achieving high Q-factors, resulting from the total internal reflection at a high refractive index contrast dielectric/environment boundary.[17,18] A large number of resonator structures support WGMs with high Q-factors including microtoroids,[19] microspheres,[20] and microdisks.[21] These WGM structures have proven to be beneficial in many applications ranging from low-threshold lasers[12,22] to optical frequency combs[23] and to environmental and particle sensors.[24] Since their realization, a significant amount of research on WGM resonators has focused on the control of the directionality of out-coupled light. This challenge originates from the fact that the high confinement results from near-unity reflection at the boundary, which makes these resonators at the same time beneficial, but at the cost of isotropic out-coupling through evanescent leakage at the boundary. It has previously been reported that, in a WGM microfiber structure, this emission can effectively be guided along the length of a coreless SiO_2 microfiber, achieving a high level of directionality thanks to strong waveguiding behavior.[12] This resonator structure is an excellent candidate for a variety of applications such as low-threshold lasers, environmental and particle sensors, biosensing, and biophotonics.

Similar to other microscale resonators, WGM microfiber cavities, however, support multiple modes, while having little control over mode discrimination with conventional techniques. Obtaining spectral purity in such cavities is fundamentally challenging and requires high precision and greater complexity of the design. Engineering stable spectral purity of multimode resonators is critical for environmental, biological and nanoparticle sensing applications.[25,26] Additional steps must be taken in order to quench competing parasitic modes. This can be achieved in a number of ways, for example, by spatially modulating the pump,[11] coupling to detuned external cavities,[27] incorporating intracavity dispersive elements such as distributed Bragg mirrors or distributed feedback gratings,[28] or extreme light confinement in subwavelength structures.[29] However, not all of these approaches are practically applicable to every class of resonators, since further constraints are introduced by each of them in terms of design, fabrication tolerance and complexity. Clearly, it is important to find alternative strategies through which mode purification can be established both in a versatile manner and without any negative impact on the overall efficiency.

Meanwhile, the capabilities of WGM resonators have made them an excellent candidate to utilize the developments of non-Hermitian and parity–time (PT) symmetric optics and photonics.[30,31] PT-symmetry was proposed in quantum mechanics as an alternative for non-Hermitian Hamiltonians $\hat{H}^{\dagger} \neq \hat{H}$, which possess a real eigenspectrum.[32] The equivalence between the electromagnetic wave equation and the Schrödinger equation in quantum mechanics has made optics an ideal platform for investigating the fundamentals of PT-symmetry,[33,34] with non-Hermiticity manifested by optical gain and loss. Investigation of PT-symmetry offers an opportunity to advance laser science by judicious manipulation of optical properties such as gain and loss, refractive index, and modal coupling to control light transport. Recently there have been reports in which colloidal quantum dots have been used as the gain media in PT-symmetric structures.[13,35] In all of these previous reports, however, the loss medium is achieved by selected pumping, where the section of the structure with the same gain material that is not excited acts as the loss medium. This method results in limitations in terms of geometrical design concepts and prevents obtaining compact devices for practical applications, where only controlled excitation is allowed.

In this work, we propose and demonstrate the ability to control the spectral purity in a microfiber-based WGM resonator enabled by all-colloidal media of both gain and loss carefully tuned for exploiting the PT symmetry-breaking concept. Here a custom-tailored nanocomposite of Ag NPs in a PMMA host is used as a loss medium with an effective complex refractive index equal to that of the CQW film in magnitude but opposite in sign at the emission peak wavelength that addresses the problems of complex pumping schemes. The coreless fiber-based WGM resonator consists of a novel PT-symmetric design. Here delicate manipulation of the gain and loss regions around the microfiber enables two energy-degenerate modes, the non-oscillating loss mode and the oscillating gain mode, whereas all higher-order modes experience a balanced gain/loss modulation, and thus remain below the lasing threshold. This unique PT-symmetric WGM cavity addresses the problem of parasitic mode competition between higher order modes and allows us to achieve a lower lasing threshold of $\approx 32\ \mu J\ cm^{-2}$ compared to the control CQW-WGM microfiber laser without PT-symmetric design. This particular cavity architecture of low-cost, all-colloidal, compact, low-threshold, directional and spectrally pure PT-symmetric WGM microfiber lasers is an excellent candidate for a wide range of applications. Benefiting from all the advantages of optical fiber sensors with stable single-mode operation, the demonstrated laser showcases a key building block for high-sensitivity environmental and particle sensors.

Results and discussion

PT-symmetry can be obtained in photonic systems if the complex refractive index distribution $n(\vec{r}) = n_R(\vec{r}) + in_I(\vec{r})$ obeys $n(\vec{r}) = n^*(-\vec{r})$.[33] Such a system can be realized in the form of a coupled arrangement with only one of the two parallel channels being optically active to provide gain for the guided light, whereas the neighbor arm experiences loss.[36] If PT-symmetry is preserved, the modes remain neutral neither decaying

nor growing. Once the gain/loss is increased beyond the coupling between two channels, this symmetry is broken, and the respective modes experience gain or loss in pairs.[36] This phenomenon of phase transition helps to control the modes in our proposed all-colloidal CQW-WGM microfiber laser.

We consider a coreless microfiber with a diameter of 125 μm coated with a 1 μm thick loss and gain medium as shown in Fig. 1a. The optical interaction between two adjacent loss/gain rings on the surface of the microfiber is mediated by the mutual overlap of their electric fields. The proposed structure creates a local PT arrangement in the radial direction, which can annihilate the higher-order competing radial WGM modes of the microfiber (see the ESI† for details).

Here we performed full electromagnetic simulations *via* a commercially available software package (Lumerical finite-difference time-domain and mode solutions). In our numerical simulations, we modeled the gain medium with a complex index (n_{CQW}) of 1.88 − *i*0.04 and the loss medium with a complex index ($n_{composite}$) of 1.88 + *i*0.04 at 650 nm according to our experimental characterization using the ellipsometry technique (see the ESI† for details). As shown in Fig. 1b, the complex eigen spectra extracted from the numerical eigenmode simulations (see the ESI† for details) of the system in the radial direction show that the rotational symmetry of the microfiber structure facilitates unique thresholdless PT-symmetry breaking, giving different modal gain and loss coefficients. Fig. 1c shows the modal intensity profile of the lasing and absorption modes in the PT-symmetric resonator. The numerical results show that the fundamental mode is in the PT-broken phase, evolving into paired lasing and absorption modes mostly distributed in the gain and loss regions, respectively. On the other hand, as shown in Fig. 1d, the higher order radial modes remain in the PT-symmetric regime, experiencing balanced gain/loss modulation and are thus suppressed below the lasing threshold. Increasing the thickness of gain and loss layers over 1 μm can make this behavior possible for higher order modes.

Fig. 1e shows the electric field intensity obtained from finite-difference time–domain (FDTD) simulations (see the ESI† for details) for the control sample with a sole 1 μm CQW gain layer around the microfiber (according to our experimental observations, lasing below 1 μm thickness is not achievable in this resonator). This geometry shows a strong evanescent field penetration into the coreless microfiber, resulting from the coupling of emission into the microfiber modes. This will result in field overlap reduction in the gain medium, deteriorating the gain performance. The modal analysis shows that four radial transverse electric modes are supported within the CQW layer around the microfiber (Fig. 1f). These modes will compete with each other resulting in multimode lasing with higher thresholds.

Here, in a PT-symmetric structure based on colloidal gain, we used an inherent loss medium based on colloidal plasmonic Ag NPs (see the ESI† for the synthesis method) integrated into a PMMA host to obtain an engineered nanocomposite

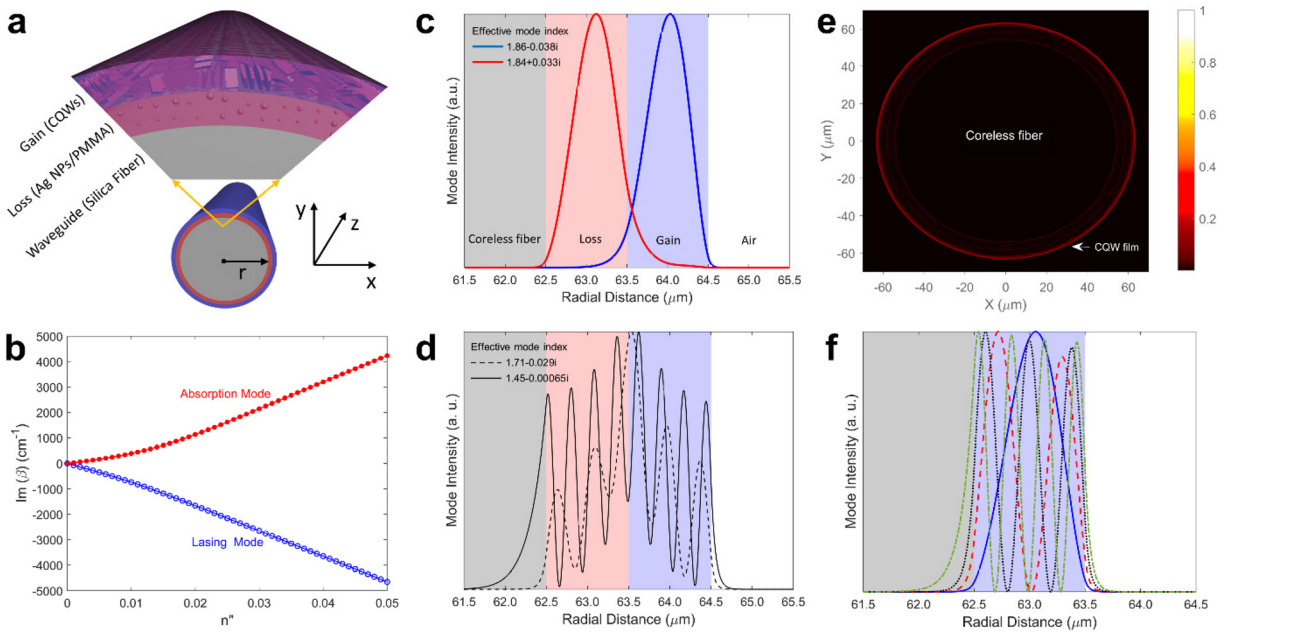

Fig. 1 (a) Schematic illustration of the PT-symmetric all-colloidal microfiber laser. The diameter of the microfiber resonator is 125 μm, and the thicknesses of the colloidal quantum well (CQW) gain layer and Ag NPs/PMMA nanocomposite loss layer are 1 μm. (b) Complex conjugate imaginary eigenspectra of the two modes as a function of the gain/loss at 650 nm determined by numerical modelling, showing a thresholdless PT-symmetry breaking. (c) Eigen-electric field intensity profiles of paired lasing and absorption fundamental modes. (d) Eigen-electric field intensity profiles of higher order modes, which are evenly distributed between the gain and loss regions. (e) Cross-sectional electric field intensity profile of the control sample with only 1 μm CQW coating around the coreless microfiber. (f) The supported eigen-electric field intensity profiles inside the 1 μm thick CQW coating in the control sample.

with the desired complex refractive index. To produce an effective medium, the diameter (D) of Ag NPs should be much smaller than the wavelength of light propagating inside this medium ($D \ll \lambda/n_{\text{eff}} = 342$ nm). As shown in Fig. 2a, the transmission electron microscopy (TEM) image of these Ag NPs features a size range smaller than 30 nm. The absorbance of Ag NP solution in toluene peaks at 410 nm (Fig. 2b), corresponding to a size of about 20 nm. The Ag NP-PMMA suspension was spin-coated on a silicon substrate with a thickness of 100–300 nm. The SEM image of the nanocomposite deposited on the silicon substrate exhibits a uniform distribution of Ag NPs in the PMMA matrix (Fig. 2c). Films with different concentrations of Ag NPs in PMMA were prepared to study the influence of concentration on the optical properties of the nanocomposite. Optical characterization was carried out by transmission measurements on the nanocomposite films deposited on transparent fused silica substrates using a commercial spectrophotometer (Cary 60 UV-Vis). The measured transmission spectra were fitted with the following equation to extract the density N (m^{-3}) of embedded Ag NPs:

$$I = I_0 \exp\left[-\alpha_0\left(1 - \frac{4}{3}\pi r^3 N\right) - (C_{\text{abs}} + C_{\text{sca}})N\right]t \qquad (1)$$

where t is the thickness of the nanocomposite, r is the radius of Ag NPs, α_0 is the extinction coefficient of the host medium (PMMA) deposited on the fused silica substrate, and C_{abs} and C_{aca} are the absorption and scattering cross-sections of Ag NPs, calculated based on Mie theory. Here, $I = I_0 \exp[-\alpha_0(1 - 4/3\pi r^3 N)]t$ defines the power absorbed or scattered by the host material excluding the volume occupied by the Ag NPs and $I = I_0 \exp[-(C_{\text{abs}} + C_{\text{sca}})N]t$ corresponds to extinction by the Ag NPs. In this way, we can approximately find the filling factor (f) of Ag NPs inside the nanocomposite. Fig. 2d shows the experimental transmission spectra of nanocomposite samples deposited on a 4 cm^2 fused silica substrate with different filling factors of Ag NPs. The nanocomposite with $f = 7.1\%$ exhibits a minimum at 430 nm due to the localized surface plasmon resonance (LSPR) phenomenon, which corresponds to a particle size of 30 nm. Considering the fact that PMMA and toluene have very close refractive indices of 1.488 and 1.493, respectively, the same LSPR wavelength in the nanocomposite film with the Ag NP solution in toluene (410 nm) was expected. The observed red shift of the LSPR wavelength in the film compared to the solution stems from a small amount of agglomeration of smaller Ag NPs. The higher red shift in other samples is an indicator of higher agglomeration, which should be avoided by a slower rate of addition of the Ag NP solution to PMMA and a longer stirring time.

For our study, CdSe/$Cd_{0.34}Zn_{0.66}S$ core alloyed hot-injection (HI) shell CQWs have been synthesized according to our recent procedure (see the ESI† for details).[11,37] To produce highly emissive, spectrally narrow, environmentally stable and near-unity efficiency core/shell CQWs, we have grown thick graded-shell on CdSe core seeds using the HI technique. These HI-grown graded-shell CQWs were shown to exhibit near-unity photoluminescence quantum yield (PL-QY) and high photo-

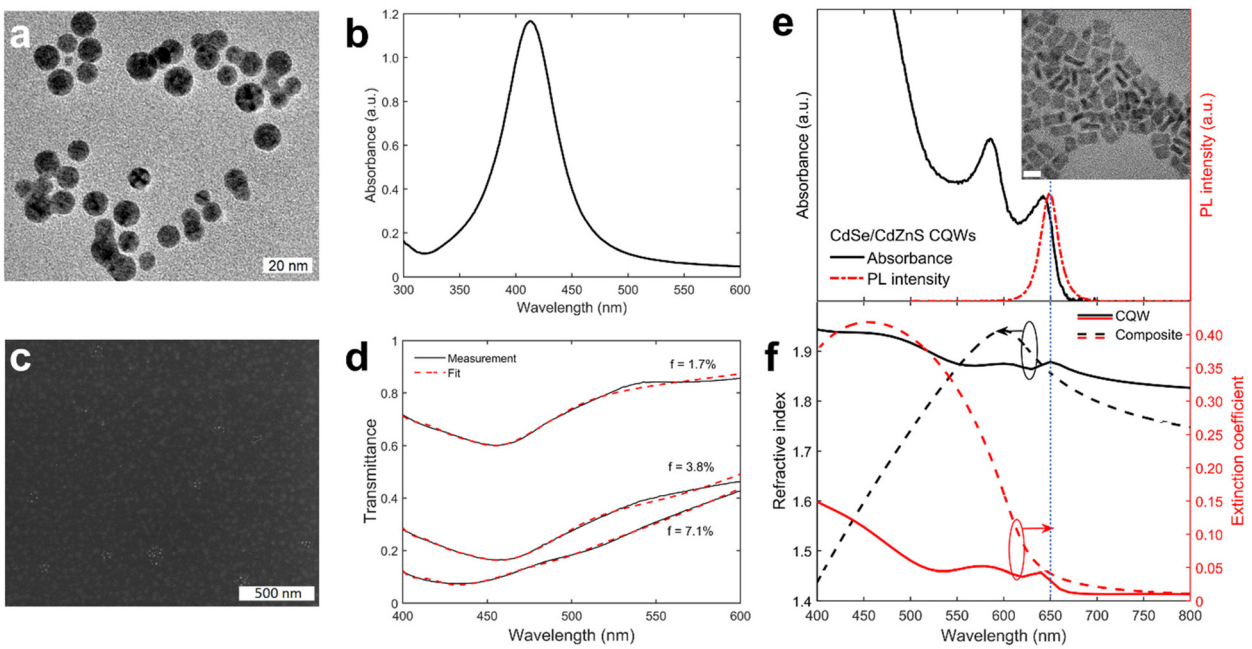

Fig. 2 (a) TEM image of plasmonic Ag NPs. (b) Absorbance of a solution of Ag NPs in toluene. (c) SEM image of the Ag NP/PMMA nanocomposite deposited on a silicon substrate. (d) Transmission spectra of the AgNPs-PMMA nanocomposite deposited on a fused silica substrate for different samples with different filling factors of Ag NPs. Black line corresponds to the experimental data and the red one corresponds to the numerical fit. (e) Photoluminescence (PL) and absorbance spectra of CdSe/$Cd_{0.34}Zn_{0.66}S$ core/HIS CQWs. Inset: High-resolution transmission electron micrograph of these CQWs (scale bar: 20 nm). (f) Effective complex refractive index of the CQW film and Ag NPs-PMMA nanocomposite ($f = 7.1\%$) film shown by solid lines and dashed lines, respectively. Black and red refer to the real and imaginary parts, respectively.

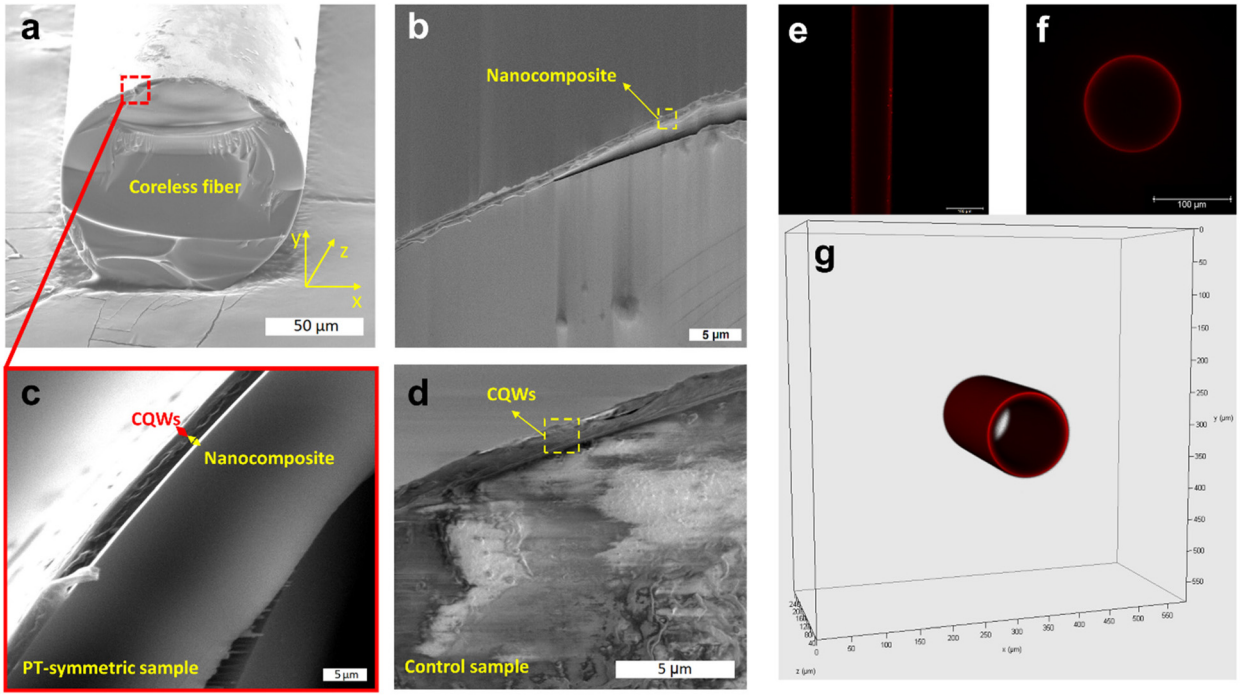

Fig. 3 (a) SEM image of the coreless microfiber coated with the Ag NPs/PMMA nanocomposite and CQWs. (b) SEM image of nanocomposite coated around the coreless microfiber (partially peeled off the microfiber surface due to the applied pressure during SEM imaging). (c) An enlarged image of the coated coreless microfiber showing the CQW and nanocomposite layers. (d) CQW coating on the coreless microfiber. PL image (e) along the axis of the microfiber at the thickest point, (f) at the cross-section normal to the axis of the microfiber, and (g) three-dimensional construction of the PL images for a length of 250 μm (obtained by confocal imaging).

and thermal-stability. The large lateral size and compositional gradient shell reduces Auger recombination and enables a low-threshold for laser action.[38] Fig. 2e PL and absorption spectra of our CQWs. The two excitonic features in the absorbance spectra located at 640 and 540 nm correspond to the electron-heavy hole and electron-light hole transitions, respectively.

The measured complex refractive index of the CQW film using ellipsometry is shown in Fig. 2f (solid lines). The complex refractive index (n_{eff}) of the Ag NPs-PMMA nanocomposite can be estimated based on the obtained f from transmission analysis, using the Bruggeman effective medium theory (EMT):[39]

$$f\frac{\varepsilon_{\text{m}}-\langle\varepsilon\rangle}{\varepsilon_{\text{m}}+2\langle\varepsilon\rangle}=(f-1)\frac{\varepsilon_{\text{PMMA}}-\langle\varepsilon\rangle}{\varepsilon_{\text{PMMA}}+2\langle\varepsilon\rangle} \quad (2)$$

where $\langle\varepsilon\rangle$ is the effective relative dielectric constant of the nanocomposite film, ε_{m} is the relative dielectric constant of Ag NPs, and $\varepsilon_{\text{PMMA}}$ is the relative dielectric constant of PMMA (Fig. S2†). The dielectric constant of Ag NPs is approximated by the Drude model, with the resulting averaged permittivity:

$$\varepsilon_{\text{m}}(\omega)=\varepsilon_{\infty}-\frac{{\omega_{\text{p}}}^2}{\omega^2+i\omega\gamma(r)} \quad (3)$$

Here the dielectric constant ε_{∞} represents the contribution of the vacuum and interband electronic transitions, ${\omega_{\text{p}}}^2 = ne^2/m\varepsilon_0$ is the bulk plasmon frequency, where n is the density of free electrons, e is the charge, and m is the mass of the electron.[40] The size-dependent damping frequency is as follows:

$$\gamma(r)=\gamma_0+A\frac{\nu_{\text{f}}}{r} \quad (4)$$

where γ_0 is the bulk damping frequency, ν_{f} is the Fermi velocity and A is the theory-dependent parameter that includes the details of the scattering process.[40] The utilized material parameters for silver are as follows: ω_{p} = 9.5 eV, ε_{∞} = 5.2, ν_{f} = 1.4 × 10^6 m s^{-1}, A = 1, and γ_0 = 0.098 eV.[41,42] Our calculations indicate that the filling factor of Ag NPs equal to f = 7.1% in a PMMA host medium gives a complex refractive index with the same real part in the magnitude as the CQW film at 650 nm, and a slightly larger imaginary part to overcome the deviations from the perfect PT-symmetry (see the ESI for details, Fig. S1 and S2†). This implies that the gain experienced in the CQW film can be balanced by the loss in the nanocomposite film.

For a proof-of-concept demonstration, we fabricated PT-symmetric CQW-WGM fiber microcavities by coating the nanocomposite and CQW layers around pieces of a coreless SiO_2 microfiber (with a diameter of 125 μm), as shown in Fig. 3a. First, a uniform film of the nanocomposite with 7.1% Ag NPs and a radial thickness of ≈ 1 μm was coated around a microfiber sample using the dip-coating technique, as shown in Fig. 3b. The thickness of this layer was controlled by dip-coating parameters (see the ESI† for details). Then, close-packed solid films of CQWs were coated *via* adhesion. Thanks

to the insoluble nature of PMMA in hexane, CQW coating on top of the composite layer by not damaging the uniformity of the AgNP-PMMA composite film is possible *via* the dip-coating method. The composite coated microfiber was dipped into a highly concentrated hexane solution of CQWs to obtain a thickness of ≈1 μm. The thickness was controlled by the concentration of this dispersion (see the ESI† for details). The SEM image in Fig. 3c confirms a uniform and layer-by-layer deposition of the nanocomposite and CQW layers consecutively. The control sample was prepared by dipping the bare coreless microfiber pieces into the CQW solution of the same concentration, which gave a thickness of ≈ 1 μm as shown in Fig. 3d. The PL reconstruction of the microfiber laser in 2D (Fig. 3e and f) and 3D (Fig. 3g) was performed with a high-resolution confocal micro-photoluminescence setup (see the ESI† for video illustration). These images clearly show that the fabricated microfiber laser has a very uniform and spotless coating over hundreds of micrometers, which will minimize the scattering losses of the supported WGM modes.

The microfiber laser was pumped with single-photon absorption (1PA) excitation (λ_{exc} = 400 nm) at ultralow excitation levels. The experimental setup is shown schematically in Fig. 4a, which shows the side-pumping scheme and depicts the directionality of the output emission (see the ESI† for details). In contrast to end pumping, side pumping is easier to handle for direct coupling. The side-pumping scheme results in a strong coupling between the gain medium and the microcavity, which is desirable for many applications, including biomedical sensors[43] and microring lasers.[12,44] Furthermore, the short round-trip-time nature of the fiber microcavity makes it easier to overcome intracavity losses and facilitates lasing. As a result, the side-pumped cylindrical microcavities can support WGMs and Fabry–Pérot (F–P) modes, both of which may have very low losses in our control sample as observed previously in semiconductor and metal–organic lasers,[44,45] while the latter will be extremely suppressed in our PT-symmetric arrangement. The coherent laser emission of the CQW-WGM microfiber laser is shown in Fig. 4b with a well-defined laser spot. Even though the emission of a WGM resonator is omnidirectional, this emission is effectively guided along the length of the SiO_2 microfiber to its end, indicating the high directionality of our microfiber-based WGM resonator.

We experimentally address the desirable features suggested by our theoretical analysis by performing quantitative analysis of the laser performance. The lasing behavior of our PT-symmetric and control samples was characterized by measuring the emission spectra from the resonators at different pump fluences, as shown in Fig. 4c. The control sample resulted in multimode lasing with a lasing threshold of 85 μJ cm^{-2}. In the PT-symmetric resonator, the lasing mode emerges above the threshold of 32 μJ cm^{-2}, creating a pronounced single-mode lasing with a full-width at half-maximum (FWHM) of ≈ 0.7 nm

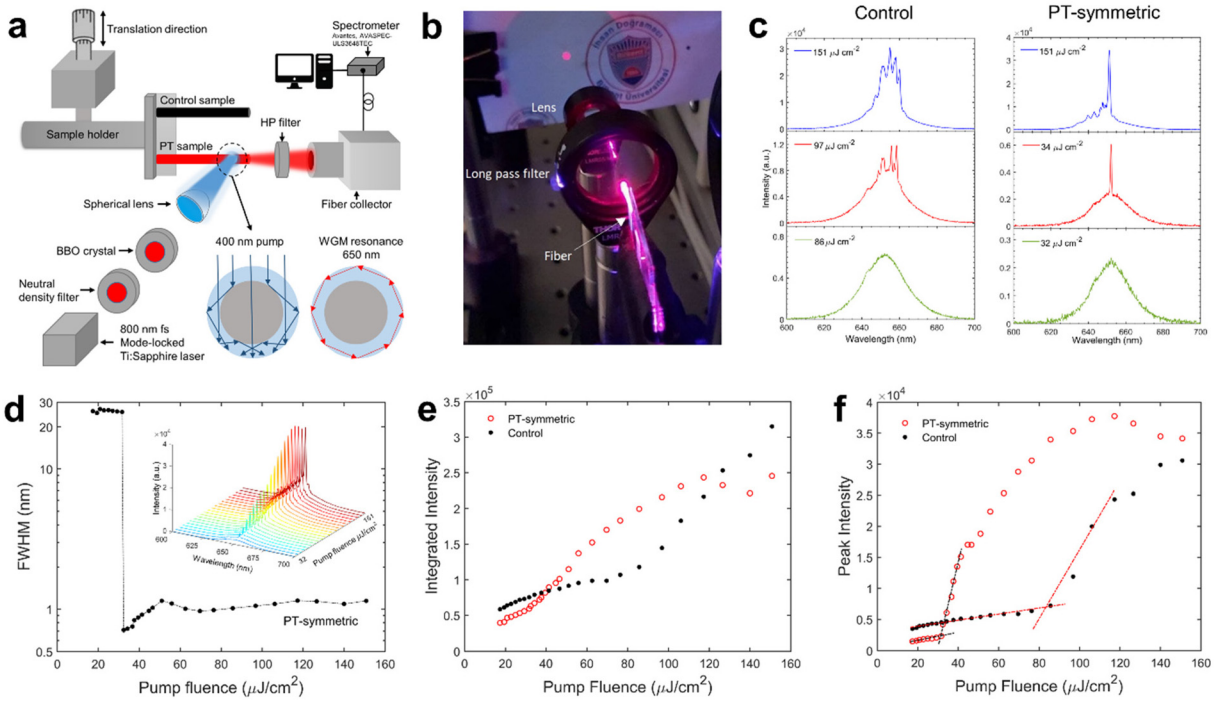

Fig. 4 (a) Schematic of the experimental setup. (b) Image of the resulting output laser spot after the long-pass filter and lens from the optically excited fiber. (c) Luminescence spectra of the control sample and PT-symmetric sample under 1PA excitation. (d) Linewidth of emission for the PT-symmetric sample extracted from Gaussian fits for the lasing spectra as a function of the pump fluence. The inset shows the measured spectra of the laser at various pumping energy densities. (e) Characteristic light–light graph of the control and PT-symmetric microfiber resonators. (f) Spectrally resolved plots comparing the intensities emitted in the desired mode from the Pt-symmetric resonator and control samples.

(the linewidths are extracted from Gaussian fits for the measured lasing spectra, see Fig. S6†) as shown in Fig. 4d, whereas other WGM modes are all below the lasing threshold and are strongly suppressed. As expected from the simulation results, in the PT-broken phase, the number of competing modes in the radial direction has reduced which results in efficient coupling of emission into the fundamental lasing mode, reducing the threshold despite introducing loss into the system. Above the threshold up to 42 μJ cm^{-2}, the operation is fully single mode. However, the PT-arrangement in the radial direction does not suppress the longitudinal WGM modes along the ring. Hence, by increasing the pump fluence further, other longitudinal WGM modes with fundamental radial mode, which are in the PT-broken phase and within the gain spectrum of the material will overcome the cavity losses and kick in (Fig. S5†). The side mode suppression ratio (SMSR) of the laser at the saturation pump fluence is ≈ 6 dB. Compared to the control sample in Fig. 4c, there is a significant improvement in the SMSR, and the number of modes has been reduced. Engineering the field distribution of the mode inside the gain medium in the radial direction has resulted in a high *Q*-factor of 930 due to the strong coupling of photons into the single fundamental mode in the radial direction in the PT-symmetry broken phase, leading to lasing threshold reduction and spectral purification compared to the control sample. In addition, the low roughness of deposited layers on the microfiber achieved over hundreds of micrometers of the length of the fiber (see the ESI† for illustration) helps in reducing scattering losses, and consequently increasing the *Q*-factor. It is also worth noting that, the threshold and quality factor may possibly be further improved by reducing the fabrication errors and surface roughness in deposition of the layers on the microfiber.

The pump fluence-dependent integrated intensity curves of control and PT-symmetric samples are shown in Fig. 4e. A characteristic change in the slope indicating that the lasing threshold can be seen with an S-curve profile of the lasing emission displaying gradual saturation at the elevated pump levels. The PT-symmetric sample shows a lower threshold and a higher level of output intensity compared to the control sample. One should note that, even in the absence of PT-symmetry, any resonator can exhibit single-mode operation, proving that the losses overcome the gain for all except one dominant mode. However, in this regime, the threshold will increase and the amplification cannot exceed the lossless resonator. In Fig. 4f, a spectrally resolved response of these two samples shows that the PT-symmetric resonator offers superior performance because the output power of the desired mode is higher, while emission from the control sample includes contributions from several modes.

The lasing threshold and spectral response of our all-colloidal PT-symmetric microfiber laser compare well with or prove better than those reported in the literature.[12] Zeng *et al.* obtained multimode lasing with a threshold of 66.5 μJ cm^{-2} in a PT-symmetry breaking design based on coupled pairs of microdisk resonators with an engineered notch fabricated from a colloidal quantum dot (CQD) gain medium.[13] Ge *et al.* obtained single mode lasing in an excitation range of 61.2–101.2 μJ cm^{-2}, when all but one of the lasing modes are suppressed by the loss μ-cavity of the PSP coupled to a fiber resonator coated with a light-emitting molecule rhodamine.[46] The demonstrated design is not operating in the PT-symmetry breaking regime, and all modes are suppressed by introducing loss into the system, which also increases the threshold compared to the case without loss. In the present work, layer by layer deposition of the all-colloidal nanocomposite and close-packed CQW smooth films in a carefully designed PT-symmetric microfiber resonator exhibits an enhancement of the laser performance.

Conclusions

By studying the lasing properties of coreless microfiber-based WGM microcavities with PT-symmetric arrangement in an all-colloidal system, we found that the coating of a balanced loss layer nanocomposite and a CQW gain layer around the microfiber results in spectral purification, as well as enhanced coupling into the gain medium resulting in low-threshold laser emission. In addition, the proposed all-colloidal PT-symmetric microfiber laser has a high level of directionality, thanks to its strong waveguiding behavior along the axis of the microfiber. In particular, the maximum achievable gain in the PT-symmetric system can be systematically enhanced with respect to competing modes. For the first time in the PT-symmetric systems using both colloidal gain and loss media, the proposed all-colloidal architecture achieves balanced inherent loss and is independent of the state of pumping. These findings indicate that this PT-symmetric colloidal design may pave the way for the use of low-cost, chemically tunable and flexible colloidal materials in lab-on-chip, sensing and low-threshold laser applications.

Conflicts of interest

Authors report no conflict of interest.

Acknowledgements

The authors acknowledge support from the Agency for Science, Technology and Research (A*STAR) MTC program, Grant No. M21J9b0085 (Singapore). The research of the project was supported by the Ministry of Education Tier 1 grant MOE-RG62/20 (Singapore). The authors thank Dr Gokce Celik for her help in the ellipsometric analyses and Ms Esra Arman for her help in the confocal microscopy imaging. The authors gratefully acknowledge the financial support in part from TUBITAK 115F297, 117E713, 119N343, 121N395 and 20AG001. H. V. D. also acknowledges the support from TUBA.

References

1 B. T. Diroll, *J. Mater. Chem. C*, 2020, **8**, 10628–10640.
2 Z. Zhang and H. Sun, *Adv. Photonics Res.*, 2021, **2**, 2100045.
3 S. Ithurria, M. D. Tessier, B. Mahler, R. P. S. M. Lobo, B. Dubertret and A. L. Efros, *Nat. Mater.*, 2011, **10**, 936.
4 A. Naeem, F. Masia, S. Christodoulou, I. Moreels, P. Borri and W. Langbein, *Phys. Rev. B: Condens. Matter Mater. Phys.*, 2015, **91**, 8–12.
5 M. Li, M. Zhi, H. Zhu, W. Y. Wu, Q. H. Xu, M. H. Jhon and Y. Chan, *Nat. Commun.*, 2015, **6**, 1–8.
6 B. Guzelturk, M. Pelton, M. Olutas and H. V. Demir, *Nano Lett.*, 2019, **19**, 277–282.
7 E. Lhuillier, S. Pedetti, S. Ithurria, B. Nadal, H. Heuclin and B. Dubertret, *Acc. Chem. Res.*, 2015, **48**, 22–30.
8 S. Foroutan-Barenji, O. Erdem, N. Gheshlaghi, Y. Altintas and H. V. Demir, *Small*, 2020, **2004304**, 1–10.
9 L. Zhang, H. Yang, B. Yu, Y. Tang, C. Zhang, X. Wang, M. Xiao, Y. Cui and J. Zhang, *Adv. Opt. Mater.*, 2020, **8**, 1–9.
10 S. Foroutan-Barenji, O. Erdem, S. Delikanli, H. B. Yagci, N. Gheshlaghi, Y. Altintas and H. V. Demir, *Laser Photonics Rev.*, 2021, **15**, 1–7.
11 N. Gheshlaghi, S. Foroutan-Barenji, O. Erdem, Y. Altintas, F. Shabani, M. H. Humayun and H. V. Demir, *Nano Lett.*, 2021, **21**, 4598–4605.
12 M. Sak, N. Taghipour, S. Delikanli, S. Shendre, I. Tanriover, S. Foroutan, Y. Gao, J. Yu, Z. Yanyan, S. Yoo, C. Dang and H. V. Demir, *Adv. Funct. Mater.*, 2020, **30**, 1–8.
13 Q. Zeng, E. Lafalce, C. H. Lin, M. J. Smith, J. Jung, Y. Yoon, Z. Lin, V. V. Tsukruk and Z. V. Vardeny, *Nano Lett.*, 2019, **19**, 6049–6057.
14 K. J. Vahala, *2005 Eur. Quantum Electron. Conf. EQEC '05*, 2005, 2005, 352.
15 T. Le, S. J. Schowalter, W. Rellergert, J. Jeet, G. Lin, N. Yu and E. R. Hudson, *Opt. Lett.*, 2012, **37**, 4961.
16 Z. Wang, Y. Ho, T. Cao, T. Yatsui and J. Delaunay, *Adv. Funct. Mater.*, 2021, **2102183**, 2102183.
17 L. He, Ş. K. Özdemir and L. Yang, *Laser Photonics Rev.*, 2013, **7**, 60–82.
18 X. J. Du, Z. J. Yang, M. L. Hu, L. Ma and J. He, *Appl. Phys. Express*, 2021, **14**, 082004.
19 D. K. Armani, T. J. Kippenberg, S. M. Spillane and K. J. Vahala, *Nature*, 2003, **421**, 925–928.
20 Y. Wang, S. Yang, H. Yang and H. Sun, *Adv. Opt. Mater.*, 2015, **3**, 652–657.
21 W. Xie, T. Stöferle, G. Rainò, T. Aubert, S. Bisschop, Y. Zhu, R. F. Mahrt, P. Geiregat, E. Brainis, Z. Hens and D. Van Thourhout, *Adv. Mater.*, 2017, **29**, 2–7.
22 Y. Wang, V. D. Ta, K. S. Leck, B. H. I. Tan, Z. Wang, T. He, C.-D. Ohl, H. V. Demir and H. Sun, *Nano Lett.*, 2017, **17**, 2640–2646.
23 P. Del'Haye, A. Schliesser, O. Arcizet, T. Wilken, R. Holzwarth and T. J. Kippenberg, *Nature*, 2007, **450**, 1214–1217.
24 J. Zhu, S. K. Ozdemir, Y. F. Xiao, L. Li, L. He, D. R. Chen and L. Yang, *Nat. Photonics*, 2010, **4**, 46–49.
25 F. Vollmer, L. Yang and S. Fainman, *Nanophotonics*, 2012, **1**, 267–291.
26 H. Xiao, S. C. Lo, Y. H. Tai, Y. L. Ho, J. K. Clark, P. K. Wei and J. J. Delaunay, *Appl. Phys. Lett.*, 2020, **116**, 161103.
27 M. W. Fleming and A. Mooradian, *IEEE J. Quantum Electron.*, 1981, **17**, 44–59.
28 K. Iga, F. Koyama and S. Kinoshita, *IEEE J. Quantum Electron.*, 1988, **24**, 1845–1855.
29 M. Khajavikhan, A. Simic, M. Katz, J. H. Lee, B. Slutsky, A. Mizrahi, V. Lomakin and Y. Fainman, *Nature*, 2012, **482**, 204–207.
30 R. El-Ganainy, K. G. Makris, M. Khajavikhan, Z. H. Musslimani, S. Rotter and D. N. Christodoulides, *Nat. Phys.*, 2018, **14**, 11–19.
31 S. K. Gupta, Y. Zou, X. Y. Zhu, M. H. Lu, L. J. Zhang, X. P. Liu and Y. F. Chen, *Adv. Mater.*, 2020, **32**, 1–32.
32 C. M. Bender and S. Boettcher, *Phys. Rev. Lett.*, 1998, **80**, 5243–5246.
33 K. G. Makris, R. El-Ganainy, D. N. Christodoulides and Z. H. Musslimani, *Phys. Rev. Lett.*, 2008, **100**, 1–4.
34 B. Peng, S. K. Özdemir, F. Lei, F. Monifi, M. Gianfreda, G. L. Long, S. Fan, F. Nori, C. M. Bender and L. Yang, *Nat. Phys.*, 2014, **10**, 394–398.
35 E. Lafalce, Q. Zeng, C. H. Lin, M. J. Smith, S. T. Malak, J. Jung, Y. J. Yoon, Z. Lin, V. V. Tsukruk and Z. V. Vardeny, *Nat. Commun.*, 2019, **10**, 1–8.
36 C. E. Rüter, K. G. Makris, R. El-Ganainy, D. N. Christodoulides, M. Segev and D. Kip, *Nat. Phys.*, 2010, **6**, 192–195.
37 Y. Altintas, U. Quliyeva, K. Gungor, O. Erdem, Y. Kelestemur, E. Mutlugun, M. V. Kovalenko and H. V. Demir, *Small*, 2019, **15**, 1–11.
38 Y. Altintas, K. Gungor, Y. Gao, M. Sak, U. Quliyeva, G. Bappi, E. Mutlugun, E. H. Sargent and H. V. Demir, *ACS Nano*, 2019, **13**, 10662–10670.
39 D. A. G. Bruggeman, *Ann. Phys.*, 1935, **416**, 636–791.
40 H. Hövel, S. Fritz, A. Hilger, U. Kreibig and M. Vollmer, *Phys. Rev. B: Condens. Matter Mater. Phys.*, 1993, **48**, 18178–18188.
41 C. Oubre and P. Nordlander, *J. Phys. Chem. B*, 2005, **109**, 10042–10051.
42 V. V. Vodnik, D. K. Božanić, N. Bibić, Z. V. Šaponjić and J. M. Nedeljković, *J. Nanosci. Nanotechnol.*, 2008, **8**, 3511–3515.
43 X. Fan and I. M. White, *Nat. Photonics*, 2011, **5**, 591–597.
44 Y. Wang, K. S. Leck, D. Van Ta, R. Chen, V. Nalla, Y. Gao, T. He, H. V. Demir and H. Sun, *Adv. Mater.*, 2014, **27**, 169–175.
45 M. Kazes, D. Y. Lewis, Y. Ebenstein, T. Mokari and U. Banin, *Mater. Res. Soc. Symp. Proc.*, 2003, **789**, 11–16.
46 K. Ge, D. Guo, B. Niu, Z. Xu, J. Ruan and T. Zhai, *Nanophotonics*, 2021, **10**, 4591–4599.